applied nano

Article

Structural and Physical Asymmetry Effects in Hyperbolic Metamaterial Waveguides

Juarez Caetano da Silva [1,2], Vitaly Felix Rodriguez Esquerre [2,*] and Zhaowei Liu [3]

1 Department of Electrotechnics, Federal Institute of Bahia, Salvador 40110-150, Brazil; jcsilva@ifba.edu.br
2 Graduate School of Electrical Engineering, Federal University of Bahia, Salvador 40210-630, Brazil
3 Electrical and Computer Engineering, University of California San Diego, La Jolla, CA 92093, USA; zhaowei@ucsd.edu
* Correspondence: vitaly.esquerre@ufba.br

Abstract

The present work analyzes light propagation in asymmetric waveguides with dielectric cores and anisotropic multilayer claddings based on nanometric planar hyperbolic metamaterials. A generalized definition of asymmetry, incorporating both structural and physical parameters, is introduced by varying metal composition and filling ratios in the claddings. The influence of wavelength, material permittivity, metal filling fraction, and core thickness on surface wave modes is examined using effective medium theory and considering experimentally derived material data. Propagation distances on the order of 400 µm have been achieved for optimized waveguide configurations operating within the C-band used in optical telecommunications.

Keywords: metamaterial waveguides; plasmonics; optics of metals

Check for updates

Academic Editors: Vittorio Scardaci and Andrei Lavrinenko

Received: 20 March 2026
Revised: 10 June 2026
Accepted: 18 June 2026
Published: 14 July 2026

1. Introduction

Optical or dielectric waveguides (WGs) play a fundamental role in integrated optics and lightwave technology for communication purposes [1,2], first, as a single-slab dielectric WG, then set up with slabs of dielectric or metal at the core or cladding areas [3–5]. Thus, a plasmonic waveguide (PW), named after the physical mechanism of wave propagation in metal-dielectric interfaces, usually has flat MIM or IMI designs, where I and M stand for insulator (dielectric) and metal, respectively. Artificially engineered multilayer composites offer new views to design WGs and other optical devices [6–18]. This kind of nanometric (or subwavelength) arrangement appears to transverse magnetic (TM) polarized radiation in the optical wavelength (λ) spectrum, as a strongly anisotropic medium with a hyperbolic dispersion relation. Anisotropic and hyperbolic metamaterials (HMMs) are subwavelength periodic structures, such as a stack of alternate I-M layers, displaying outstanding design and functional abilities. Taking into account their singular optical response, HMM has been used not only as PW-WG claddings, exhibiting better performance than conventional isotropic slab MIM-PW or IMI-PW devices [6–18], but also in recent designs of common coupler-WG pairs [6], as well as very new structures like metasurfaces [7]. Consequently, HMMs enable the design of on-chip, nanoscale optical devices with unprecedented electromagnetic properties. Furthermore, they pave the way for merging two leading technologies: CMOS and nanophotonics [19]. Recent advances in thin-film technology, fabrication, and characterization techniques support these expectations [19–28], resulting in the proposal of new waveguide configurations: In [24], two dielectric-coated Na nanowires—composed of cylindrical Na nanowires with one or two dielectric cladding layers—were investigated. In [25], a nickel-based elliptical-cylinder plasmonic nanowaveguide with a propagation length exceeding 470 μm was presented. In [26], a cylindrical composite hybrid plasmonic waveguide was introduced that supports a plasmon mode with ultra-strong field confinement. This mode is formed through the coupling between the surface plasmon mode in the Na nanowire waveguide and the hybrid surface plasmon mode in the Na-based cylindrical hybrid waveguide at 1550 nm.

A palladium-based elliptical-cylinder plasmonic waveguide was analyzed in [27], achieving an excellent propagation length greater than 270 μm in the near-infrared (NIR) range. In [28], a multilayer graphene metamaterial plasmonic waveguide with ultra-low loss was proposed for the mid-infrared range, where the designed structure supports an SPP mode with a propagation length close to 100 μm. Finally, in [29], a waveguide structure combining a high-index cylindrical dielectric at the coordinate origin, a low-index dielectric strip, and a monolayer graphene sheet surrounded by a SiO_2 rectangular cube was studied. The modal characteristics of the graphene surface plasmon polariton (SPP) mode were analyzed using the finite element method, and the results showed a propagation length of approximately 100 μm.

Here, we classify WGs based on the propagation length (L) that light experiences when interacting with boundaries. To simplify the description of these asymmetric structures, our numerical model uses a one-dimensional (1D) approach using the effective medium theory [30]. Planar HMM structures predominate here since they are the most feasible architecture for nanoscale device fabrication [19–23]. In view of this, we alter the structural meaning of asymmetry [6–23,31–33] in a straightforward manner, i.e. varying not only the metal filling ratios (r)but also the very metal nature in each multilayer. Thus, we are merging the usual sense of asymmetry with that one proper to all-dielectric slab WGs, leading to a multitude of HMM-WGs designs. Our results may be regarded as an expressive demonstration of the wide performance and versatility that full-asymmetry HMM-WG reveals.

This paper is organized as follows. Section 2 deals with theoretical background and material specifications that support the numerically based approach. Section 3 is dedicated to presenting and commenting on simulation results. Section 4 is devoted to the conclusion pointing to future works.

2. Theoretical Formalism and Constituent Aspects

The theoretical method usually adopted to describe HMM optical properties embraces an effective medium theory (EMT) [11–23,30–33]. At this point, this means that planar HMM must have proper subwavelength film dimensions with respect to working wavelength λ, where homogeneous optical response takes place. This is the EMT regime in which we find out the effective parameters required to model HMM as homogeneous and anisotropic media. An approach extensively used to study HMM–Insulator–HMM (HIH) waveguides here [6–23,31,32]. The EMT approximates the multilayered structure as an equivalent homogeneous medium, which is valid when the individual layer thicknesses and the overall period of the multilayer are much smaller than the operating wavelength. Although full-wave simulations of the complete multilayered configuration are beyond the scope of the present work, previous studies [9–14] have demonstrated that EMT provides a reliable approximation for propagation length calculations in similar hyperbolic metamaterial waveguides. Therefore, the EMT-based analysis employed here is expected to accurately compute the length propagation characteristics of the proposed structure. The optical constants have been obtained from [34–38]. As our first material choice, silver (Ag) is the HMM metal due to its low ohmic losses. Then we test gold (Au) as another HMM component, a choice oriented by the low chemical reactivity of Au [29]. We assume dissipative metal with complex dielectric function ε_m and real ε_d = 2.1025 for silica (SiO_2). In practical implementations, metallic losses are typically higher than those predicted by idealized theoretical models due to fabrication imperfections, surface roughness, grain boundaries, and deviations in the experimental dielectric response of metals. Furthermore, although air is considered in part of our analysis, we also investigated other dielectric core materials. Lossy core materials may introduce additional absorption losses; both effects increase the imaginary part of the effective refractive index, leading to a reduction in the propagation length.

HIH-WGs have air (ε_c = 1.0), magnesium fluoride (MgF_2, ε_c = 1.878) or ε_c = 1.4 core constituents. The last one works as an intermediate ε_c, improving our analyses. Figure 1a is a schematic view of the planar HIH-WG, and Figure 1b is the equivalent EMT model. In order to avoid any confusion and for the sake of simplicity, we assign to Figure 1b three regions i = 1, 2, 3 from top to bottom, respectively. The HIH-WG model is described by a few parameters, that is, core width d and cladding metal filling ratio $r = d_m/(d_m + d_d)$ between the total metal layer thickness d_m and dielectric d_d counterpart. Two basic HIH-WGs assemblies are possible. A symmetric one with the same r_i (i = 1,3) and an asymmetric one with different r_i (i = 1,3) are used for the upper and bottom claddings. The first device has been extensively analyzed. The last one is considered in this work.

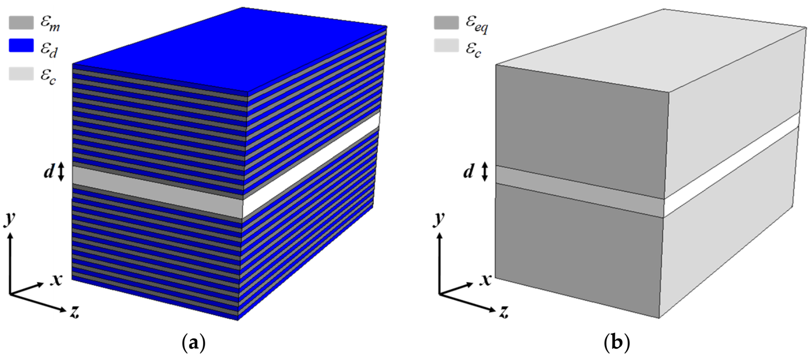

Figure 1. HIH-WG schematic view (**a**) multilayered cladding and (**b**) equivalent anisotropic homogeneous cladding.

Homogeneous and isotropic insulators have $\bar{\epsilon} = diag(\varepsilon_c, \varepsilon_c, \varepsilon_c)$ tensor representation with real and positive ε_c components. On the other hand, the HMM tensor model has $\bar{\epsilon} = diag(\varepsilon_x, \varepsilon_y, \varepsilon_z)$ and uniaxial symmetry, that is, equal parallel $\varepsilon_x = \varepsilon_z$ and perpendicular ε_y interface components. The relationship between ε_m, ε_d, and HMM tensor components arises from the EMT approach. Here, the propagation geometry assumes surface plasmon polariton (SPP) waves propagating in the x direction and no spatial variation in the in-plane z direction ($\frac{\partial}{\partial z} = 0$). For our 1D problem, the SPP wave has a parallel propagation constant k_x and perpendicular $k_{y,i}$ (i = 1, 2, 3) interface wave vector components. Employing $\varepsilon_\perp = \varepsilon_y$ and $\varepsilon_\parallel = \varepsilon_x = \varepsilon_z$ notation, the uniaxial HMM tensor $diag(\varepsilon_\parallel, \varepsilon_\perp, \varepsilon_\parallel)$ component reads [20,31]:

$$\varepsilon_\perp = \varepsilon_y = \varepsilon_m \varepsilon_d / ((1-r)\varepsilon_m + r\varepsilon_d),\ \varepsilon_\parallel = \varepsilon_x = \varepsilon_z = (1-r)\varepsilon_d + r\varepsilon_m. \quad (1)$$

If we select different HMMs for Figure 1b, in three layers, the dispersion relationship for this full HMM-WG reads [3,9–12]:

$$\tanh(2k_{y,2}d) = -\frac{(k_{y,2}/\varepsilon_{x,2})(k_{y,1}/\varepsilon_{x,1} + k_{y,3}/\varepsilon_{x,3})}{(k_{y,2}/\varepsilon_{x,2})^2 + (k_{y,1}/\varepsilon_{x,1})(k_{y,3}/\varepsilon_{x,3})}, \quad (2)$$

with the implicit relation $k_{y,i} = \sqrt{\varepsilon_{y,i}^{-1}\varepsilon_{x,i}k_x^2 - \varepsilon_{x,i}k_0^2}$($i$ = 1, 2, 3) connecting $k_{y,i}$ and k_x appearing above [3,9–12]. The general form of Equation (2) (and $k_{y,i}$) will be the sources of desired relations, as follows.

Asymmetric HIH-WG implies $\varepsilon_{x,2} = \varepsilon_{y,2} = \varepsilon_c$ and $k_{y,2} = \sqrt{k_x^2 - \varepsilon_c k_0^2}$ in Equation (2) (and $k_{y,i}$). Although common, an insulated core not only defines but also makes this choice the better one to study the length propagation over the propagation character of our unusual WG devices. The dispersion relation to be numerically calculated (see Section 3) reads [3,9–12]:

$$\tanh(2k_{yc}d) = -2\frac{(k_{yc}/\varepsilon_c)(k_{yH}/\varepsilon_x)}{(k_{yc}/\varepsilon_c)^2 + (k_{yH}/\varepsilon_x)^2}, \quad (3)$$

Symmetric HIH-WGs are expected to perform the following function first. Since no other authors, to our knowledge, explored the asymmetries effects in metamaterial waveguides, we cannot compare our results with previously published works. However, we validated our approach with symmetric waveguides. Symmetric HIH-WGs have another $k_{y,i}$ form.

Now $\varepsilon_{x,2} = \varepsilon_{y,2} = \varepsilon_c$, $k_{y,2} = \sqrt{k_x^2 - \varepsilon_c k_0^2}$ at the core and $\varepsilon_{x,i} = \varepsilon_x$ $\varepsilon_{y,i} = \varepsilon_y$ i = (1,3), $k_{y,1} = k_{y,3} = \sqrt{\varepsilon_x\left(\varepsilon_y^{-1}k_x^2 - k_0^2\right)}$ at claddings. Thus, Equation (3) simplifies [9–11]:

$$\tanh(k_{y,2}d) = -k_{y,1}\varepsilon_c/\varepsilon_x k_{y,2} \quad (4)$$

A direct measure of energy decrease in the direction of propagation is defined as $L = \mathrm{Im}(2k_x)^{-1}$. This formula also reveals, via k_x, the physical meaning of L dependence with regard to d, r, and ε_c WG parameters. As already explained, the propagation length L will be used to gauge the performance of the asymmetry effects in HIH-WG devices. A direct measure of the mode profile at the interfaces is defined as $d_p = \left(2k_0\mathrm{Im}\left[k_y\right]\right)^{-1}$. Although out of the main scope of this paper, the penetration depth defined above is another reason why multilayered WG are preferable to the traditional ones.

Metal and insulator experimental optical constants are due to references [31–34]. Incident light within 1200 nm $\leq \lambda \leq$ 1700 nm or λ = 1550 nm (C-band telecom standard) midpoint is observed in our simulations. The analysis proceeds with $0.2 \leq r_i \leq 1$ (i = 1,3) as well as fixed r_3 or fixed d WG layouts. HIH-WG cores have d = 25 nm up to d = 75 nm, another interval than that used to study both symmetric and asymmetric HIH-WGs [9–11]. Smaller d is in the order of magnitude of the thinnest Au layer that can be deposited on a silica substrate [22]. Also, we generalize the characterization of asymmetry ($r_1 \neq r_3$), selecting different metals for each HMM cladding. The next section is dedicated to looking at some singular L behavior in these devices.

3. Results and Discussion

We first assume full-asymmetric ($r_1 \neq r_3$) $0.1 \leq r_i \leq 1$ (i = 1,3) $AgSiO_2$ HIH-WGs under λ = 1550 nm radiation. Three ε_c are considered: 1.0 (a, d), 1.4 (b, e), and 1.878 (c, f) columns with upper rows, d = 50 nm, and bottom rows, d = 75 nm in Figure 2. The figure displays L dependence on them. We considered in our simulations waveguides with core widths compatible with those found in the specialized literature analyzing metamaterial waveguides operating in the infrared interval of frequencies of about tens of nanometers.

Figure 2 shows that larger d corresponds to larger L, regardless of ε_c or r_i. Further, d insensibility (L constant) occurs when $r_i \geq 0.4$ (i = 1,3) accompanied by L decreasing as ε_c increases. More homogeneous behavior happens in Figure 2c,f (ε_c = 1.878), $r_i \geq 0.2$ (i = 1,3), but with a smaller L. Thus, fixing ε_c and L operation point, one has HIH-WG designs unveiling the r_i-tolerant devices (λ = 1550 nm).

As r_i goes to unity, a symmetric MIM-WG limiting case arises, usually reducing the propagation length to pay off the dissipative metal presence in the structure. It is easy to see in Figure 2a,d (ε_c = 1.0) that this is not the case for full-asymmetric AgSiO2 HIH-WGs.

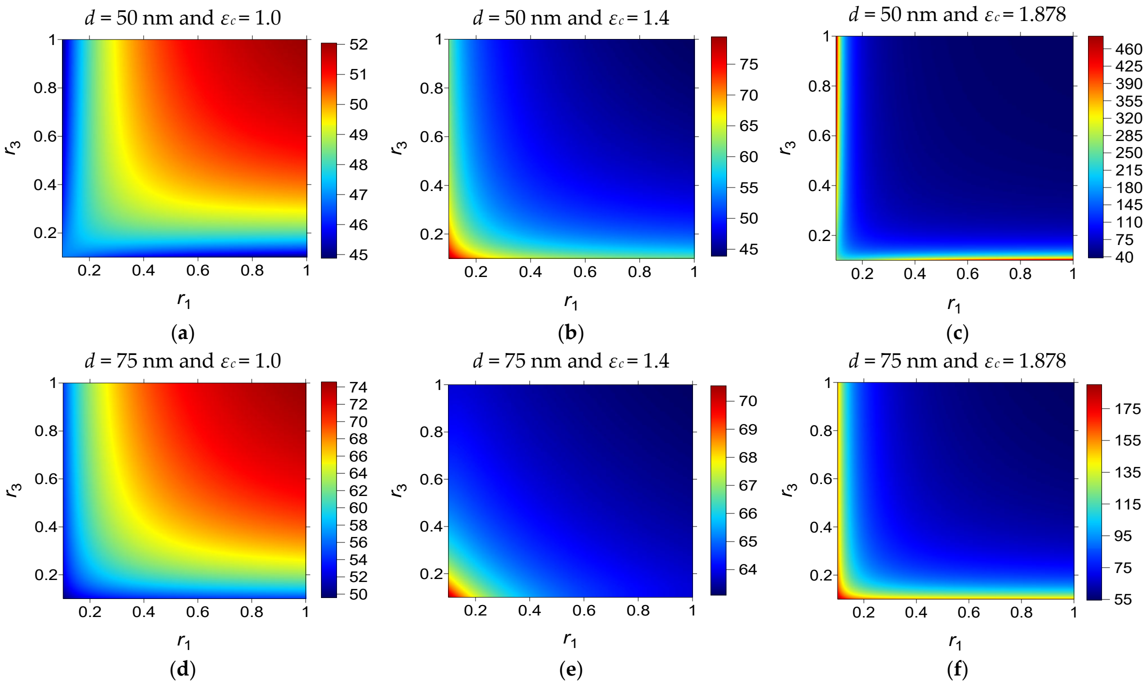

Figure 2. L in full-asymmetric $AgSiO_2$ HIH-WG, λ = 1550 nm. The waveguide parameters are (**a**) d = 50 nm and ε_c = 1.0; (**b**) d = 50 nm and ε_c = 1.4; (**c**) d = 50 nm and ε_c = 1.878; (**d**) d = 75 nm and ε_c = 1.0; (**e**) d = 75 nm and ε_c = 1.4; (**f**) d = 75 nm and ε_c = 1.878.

In fact, another unexpected feature occurs with L increasing while r_i increases, showing the strong correlation between r_i, ε_c, and d that (λ = 1550 nm) light perceives in these structures. Above $r_i \geq 0.4$ (i = 1,3), a constant L profile is assured for all devices, which always depends on d and ε_c values.

The next step studies full-asymmetric ($r_1 \neq r_3$) $0.1 \leq r_i \leq 1$ (i = 1,3) $AuSiO_2$ HIH-WGs under λ = 1550 nm radiation. Figure 3 has ε_c: 1.0 (a, d), 1.4 (b, e), and 1.878 (c, f) columns with upper d = 50 nm and bottom d = 75 nm rows. The figure displays L dependence on them.

Figure 3 reproduces all the L behavior displayed in Figure 2, but with a smaller L. The more dissipative optical properties of Au than those of Ag reduce the L propagation length in $AuSiO_2$ assemblies. Even so, the low chemical reactivity of Au may overcome this unfavorable response in applications like open-air sensor systems [35]. Nevertheless, L performance measured in tens of μm always achievable.

Common sense of asymmetry ($r_1 \neq r_3$) can be generalized in a straightforward manner, taking Au as the upper and Ag as the bottom multilayer metal elements. For the sake of comparison with the WG undergone conventional asymmetry, such a full-asymmetric $AgAuSiO_2$ HIH-WG was simulated, mirroring (λ = 1550 nm, $0.1 \leq r_i \leq 1$, $i = 1, 3$) previous ones. Thus, Figure 4 has ε_c = 1.0 (a, d), 1.4 (b, e), and 1.878 (c, f) columns with upper d = 50 nm and bottom d = 75 nm rows. The figure presents singular L performances still not discussed.

Figure 4 displays a more involved dependence of L on r, d, and ε_c changes. All columns indicate ubiquitous L increasing as d increases from the upper to the bottom rows. Simultaneously, all rows indicate L decreasing as ε_c increases from Figure 4a,d to Figure 4c,f columns. Whereas better uniformity and insensibility (L constant) to r_{i} (i = 1,3) arises as ε_c increases in both d rows. So, one has new designs unveiling a new r_i-tolerant fabrication issue (λ = 1550 nm). There are a couple of singular behaviors to assert for L now. Fixing L and d operating point, r_i (i = 1,3) region-free occurs at a narrow ($0.7 \leq r_i \leq 1$) or larger ($0.4 \leq r_i \leq 1$) range in Figure 4a,d (ε_c = 1.0), and Figure 4c,f (ε_c = 1.878), respectively. Conversely, fixing ε_c and d operating point, r insensibility (constant L) profile appears only to specific r_1 interval. As an example, Figure 4d (ε_c = 1.0) presents narrower ($0.4 \leq r_1 \leq 0.7$)

https://doi.org/10.3390/applnano7030020

while Figure 4f (ε_c = 1.878) presents wider ($0.4 \leq r_1 \leq 1$) (d = 75 nm) fabrication tolerance. Figure 4b,e are clear examples of what a full-asymmetric design can offer. We can see that the mean ε_c operating point relates to noticeable equidistant L behavior.

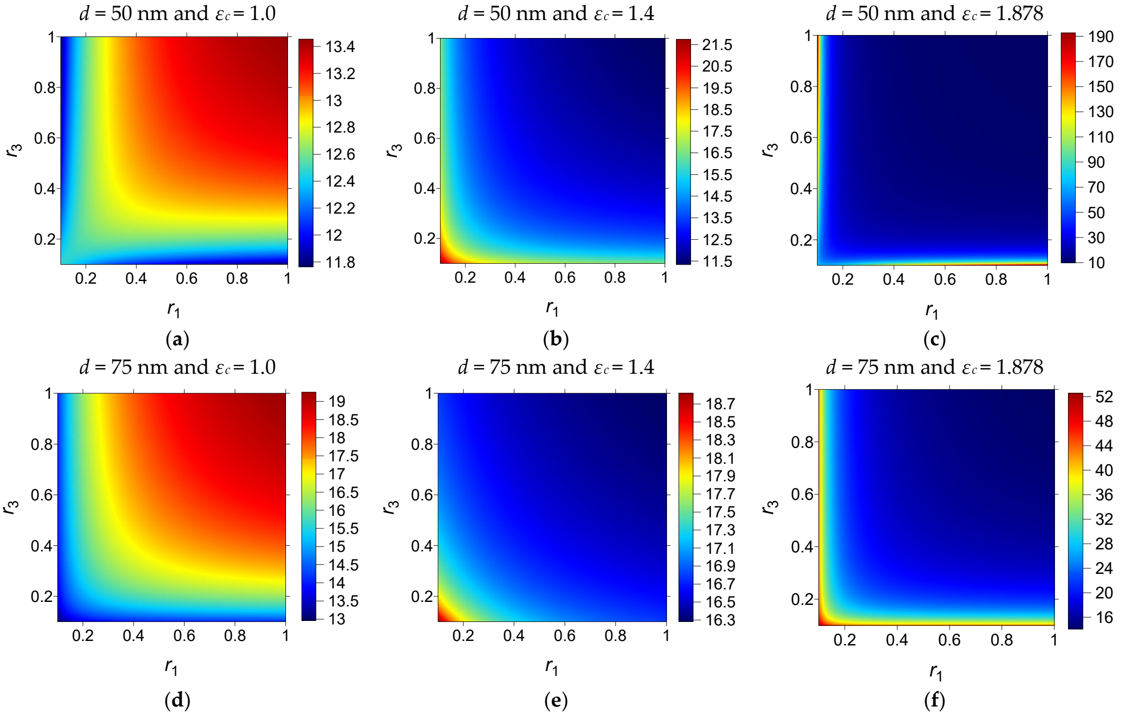

Figure 3. L in full-asymmetric $AuSiO_2$ HIH-WG, λ = 1550 nm. The waveguide parameters are (**a**) d = 50 nm and ε_c = 1.0; (**b**) d = 50 nm and ε_c = 1.4; (**c**) d = 50 nm and ε_c = 1.878; (**d**) d = 75 nm and ε_c = 1.0; (**e**) d = 75 nm and ε_c = 1.4; (**f**) d = 75 nm and ε_c = 1.878.

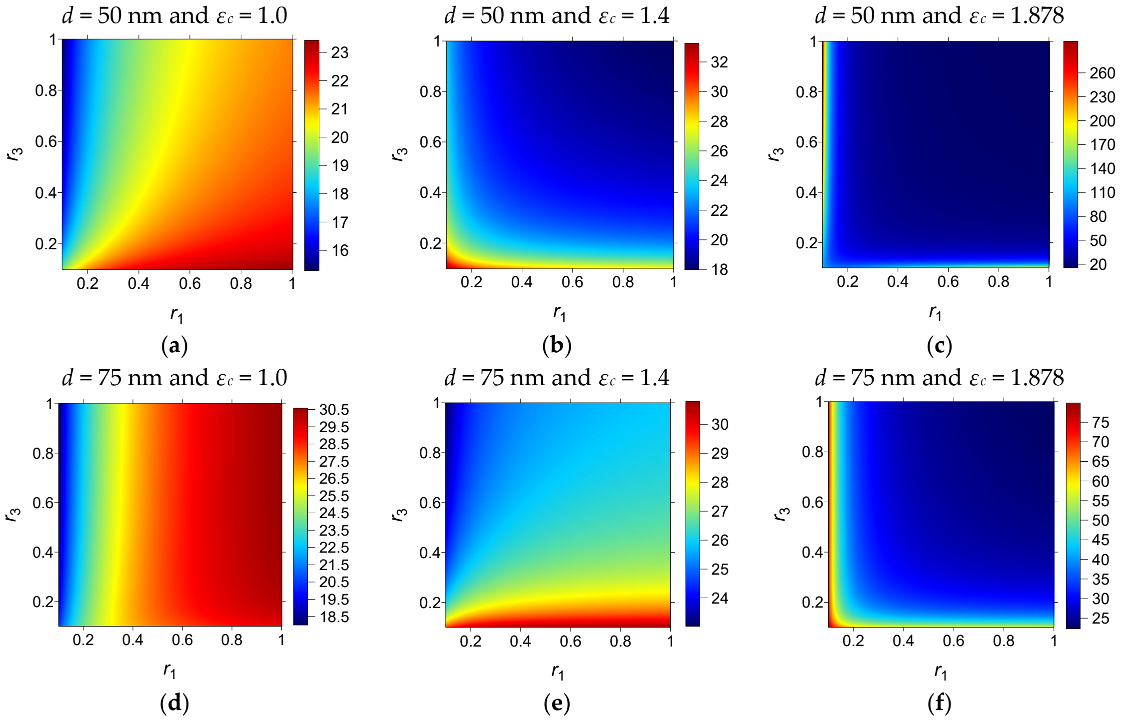

Figure 4. L in full-asymmetric $AgAuSiO_2$ HIH-WGs, λ = 1550 nm. The waveguide parameters are (**a**) d = 50 nm and ε_c = 1.0; (**b**) d = 50 nm and ε_c = 1.4; (**c**) d = 50 nm and ε_c = 1.878; (**d**) d = 75 nm and ε_c = 1.0; (**e**) d = 75 nm and ε_c = 1.4; (**f**) d = 75 nm and ε_c = 1.878.

Planar HMM flexibility now takes the form of restricted structural asymmetry (fixed d or r_3). Restrict asymmetry 1D architecture is a simple and powerful model employed here to investigate L spectral response (1200 nm $\leq \lambda \leq$ 1700 nm). Initially, in $AgAuSiO_2$ HIH-WGs with r_3 = 0.5 ($\varepsilon_{m3} = \varepsilon_{Ag}$) as a suitable midpoint of metal presence in the bottom cladding, while 0.2 $\leq r_1 \leq$1 ($\varepsilon_{m1} = \varepsilon_{Au}$) runs freely. Figure 5 has ε_c = 1.0 (a, d, g), 1.4 (b, e, h), and 1.878 (c, f, i) columns with d = 25 nm, d = 50 nm, and d = 75 nm upper, middle, and bottom rows, respectively. In the following, broadband WGs can operate over the complete optical communications frequencies, covering from 1200 nm to 1700 nm. On the other hand, narrowband will maintain its propagation characteristics in less than half of the broadband ones.

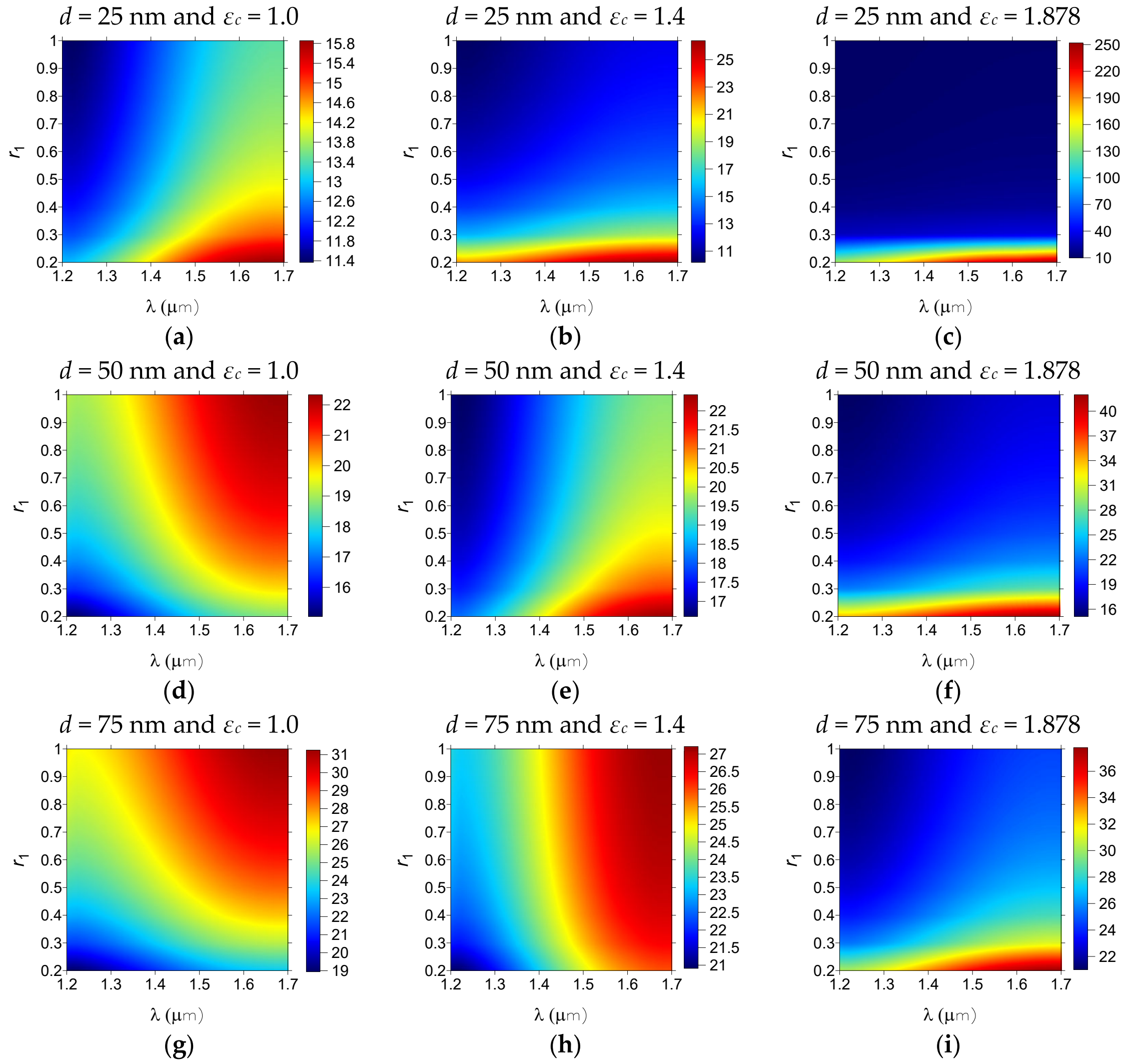

Figure 5. L in fix-asymmetric (r_3 = 0.50) $AgAuSiO_2$ HIH-WG. The waveguide parameters are (**a**) d = 25 nm and ε_c = 1.0; (**b**) d = 25 nm and ε_c = 1.4; (**c**) d = 25 nm and ε_c = 1.878; (**d**) d = 50 nm and ε_c = 1.0; (**e**) d = 50 nm and ε_c = 1.4; (**f**) d = 50 nm and ε_c = 1.878; (**g**) d = 75 nm and ε_c = 1.0; (**h**) d = 75 nm and ε_c = 1.4; (**i**) d = 75 nm and ε_c = 1.878.

Above $r_1 \geq$ 0.4 and $\lambda \geq$ 1400 nm, Figure 5c,f,i (ε_c = 1.878) shows HIH-WGs owing to d insensibility (L constant) behavior. Regarding λ, this can be thought of as broadband devices. In contrast, under specific d and ε_c operating point, Figure 5a,d,g (ε_c = 1.0) and Figure 5b,e,h (ε_c = 1.4) show narrowband ones above $r_1 \geq$ 0.5. For example (ε_c = 1.4, d = 50 nm), operating pointing defines a constant L profile HIH-WG to $\lambda \geq$ 1500 nm radiation. Others' narrowband designs result from choosing a new (ε_c = 1.4, d = 75 nm) operating point. This way, L = 25 μm (1550 nm $\leq \lambda \leq$ 1600 nm) or L = 30 μm ($\lambda \geq$ 1600 nm) behavior takes place. As always, L performance has deeply dependence on r_1, λ, and ε_c parameters.

Restrict asymmetry also applies to $AuAgSiO_2$ HIH-WG, r_3 = 0.50 ($\varepsilon_{m3} = \varepsilon_{Au}$), bottom cladding, while $0.2 \leq r_1 \leq 1$ ($\varepsilon_{m1} = \varepsilon_{Ag}$) runs freely, maintaining λ of the previous regime. Figure 6 has ε_c = 1.0 (a), 1.4 (b), and 1.878 (c) columns with d = 25 nm, d = 50 nm, and d = 75 nm upper, middle, and bottom rows, respectively.

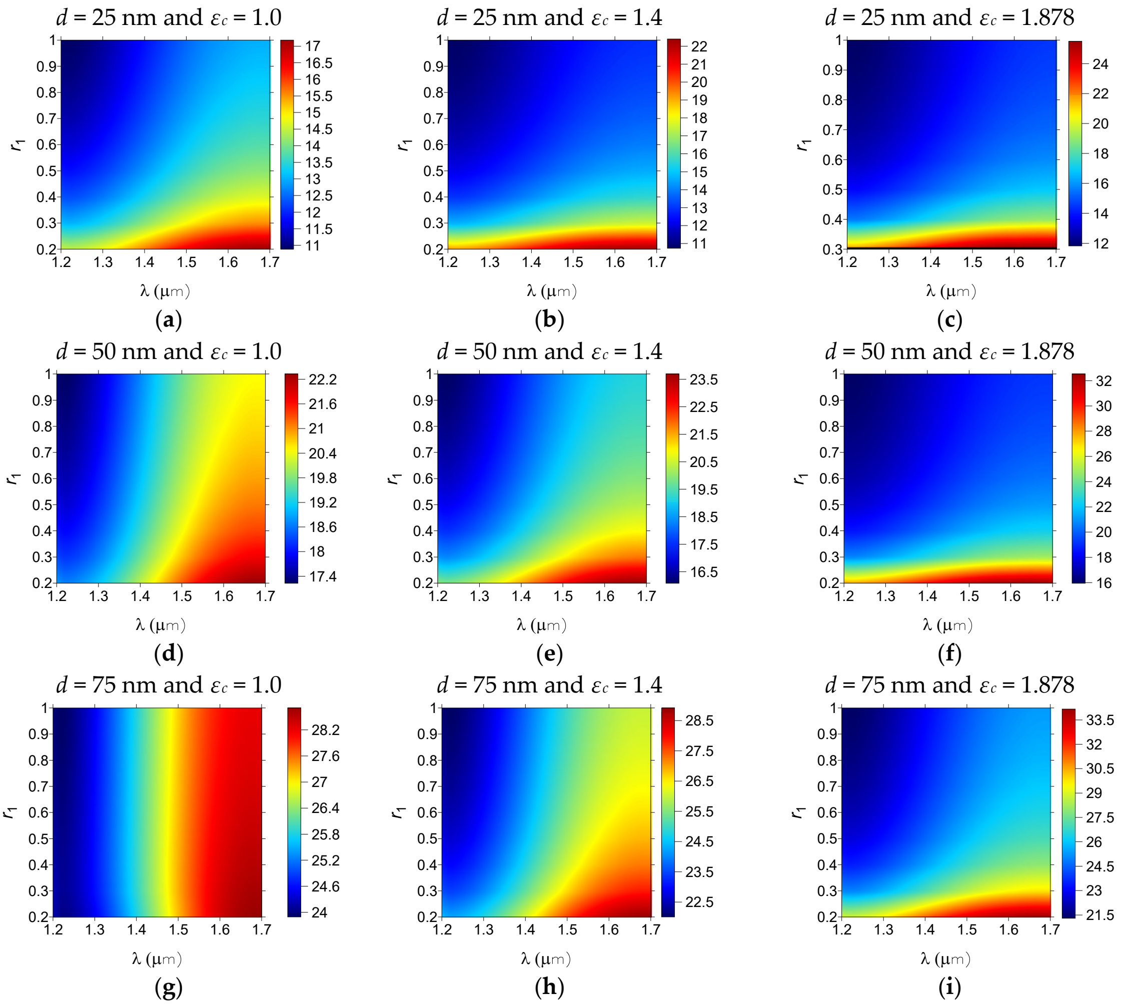

Figure 6. L in fix-asymmetric (r_3 = 0.50) $AuAgSiO_2$ HIH-WG. The waveguide parameters are (**a**) d = 25 nm and ε_c = 1.0; (**b**) d = 25 nm and ε_c = 1.4; (**c**) d = 25 nm and ε_c = 1.878; (**d**) d = 50 nm and ε_c = 1.0; (**e**) d = 50 nm and ε_c = 1.4; (**f**) d = 50 nm and ε_c = 1.878; (**g**) d = 75 nm and ε_c = 1.0; (**h**) d = 75 nm and ε_c = 1.4; (**i**) d = 75 nm and ε_c = 1.878.

Figure 6c (ε_c = 1.878) and Figure 6b (ε_c = 1.4), d = 25 nm single $r_1 \geq 0.5$, $\lambda \geq$ 1450 nm regions, define HIH-WGs owing to d insensibility (L constant) response. Regarding λ, these designs can be thought of as broadband devices. In contrast, Figure 6a,d,g (ε_c = 1.0) as well as Figure 6e,f (ε_c = 1.4) ($d \geq$ 50 nm) displays a constant L profile only above $r_1 \geq 0.4$, always in narrow λ intervals (see Figure 6g, d = 75 nm). So we have a set of narrowband HIH-WGs to complete a wide selection of L performances that the planar HIH-WG project makes possible. At different L levels, Figure 6 reproduces what Figure 5 displays.

Another way to explore restricted asymmetry in WGs takes a fixed d = 30 nm, for example, with different ε_c, r_3 pairs, while $0.1 \leq r_1 \leq 1$ runs freely. Figure 7 has ε_c = 1.0 (a, d, g), 1.4 (b, e, h), 1.878 (c, f, i) columns crossing r_3 = 0.25, r_3 = 0.50, r_3 = 0.75 upper, middle, and bottom rows, respectively. Simulated L spectral response (1200 nm $\leq \lambda \leq$ 1700 nm) results for $AgAuSiO_2$ HIH-WG with new structural condition are shown in Figure 7.

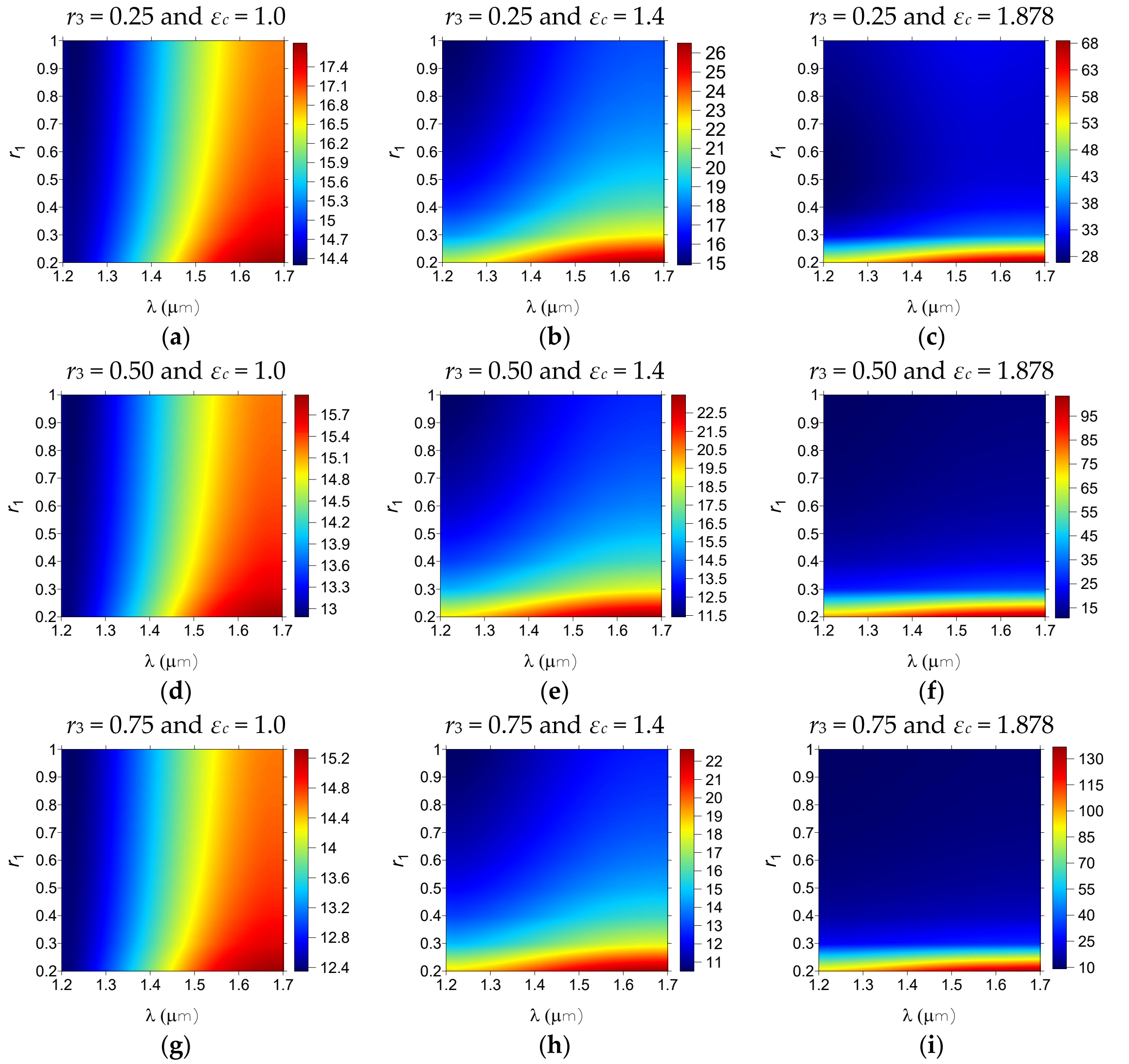

Figure 7. L in fix-asymmetric $AgAuSiO_2$ HIH-WG with fixed d = 30 nm. The waveguide parameters are (**a**) r_3 = 0.25 and ε_c = 1.0; (**b**) r_3 = 0.25 and ε_c = 1.4; (**c**) r_3 = 0.25 and ε_c = 1.878; (**d**) r_3 = 0.50 and ε_c = 1.0; (**e**) r_3 = 0.50 and ε_c = 1.4; (**f**) r_3 = 0.50 and ε_c = 1.878; (**g**) r_3 = 0.75 and ε_c = 1.0; (**h**) r_3 = 0.75 and ε_c = 1.4; (**i**) r_3 = 0.75 and ε_c = 1.878.

Figure 7c (ε_c = 1.878) and Figure 7b (ε_c = 1.4) single $r_1 \geq 0.4$, $\lambda \geq$ 1350 nm regions, define HIH-WG owing to r_3 insensibility (L constant) response. Regarding λ, these designs can be thought of as broadband devices. In contrast, Figure 7a,d,g (ε_c = 1.0) ($r_3 \geq 0.25$) only displays L constant profile above $r_1 \geq 0.3$ always in narrow λ intervals ($\lambda \geq$ 1550 nm). These designs can be thought of as narrowband devices. Restrict asymmetry fixed d shows better L performance HIH-WGs than fixed r_3 ones. Finally, the asymmetry d = 30 nm $AuAgSiO_2$ HIH-WGs ($\varepsilon_{m3} = \varepsilon_{Au}$) was simulated using identical parameters describing the last structures. Thus, Figure 8 has ε_c = 1.0 (a, d, g), 1.4 (b, e, h), 1.878 (c, f, i) columns crossing r_3 = 0.25, r_3 = 0.50, and r_3 = 0.75 upper, middle, and bottom rows, respectively.

Figure 8f,i (ε_c = 1.878) HIH-WG owing to r_3 insensibility (L constant) response. With regards to λ, only these designs can be thought of as broadband devices. The other ones only show the L constant profile in narrow λ and r_1 intervals. So, restrict asymmetry

d = 30 nm $AuAgSiO_2$ HIH-WGs are essentially narrowband devices, at least in the interval of 1200 nm $\leq \lambda \leq$ 1700 nm illumination.

Figure 8 corroborates that fixed d asymmetry HIH-WGs have better L performance than fixed r_3 similar designs.

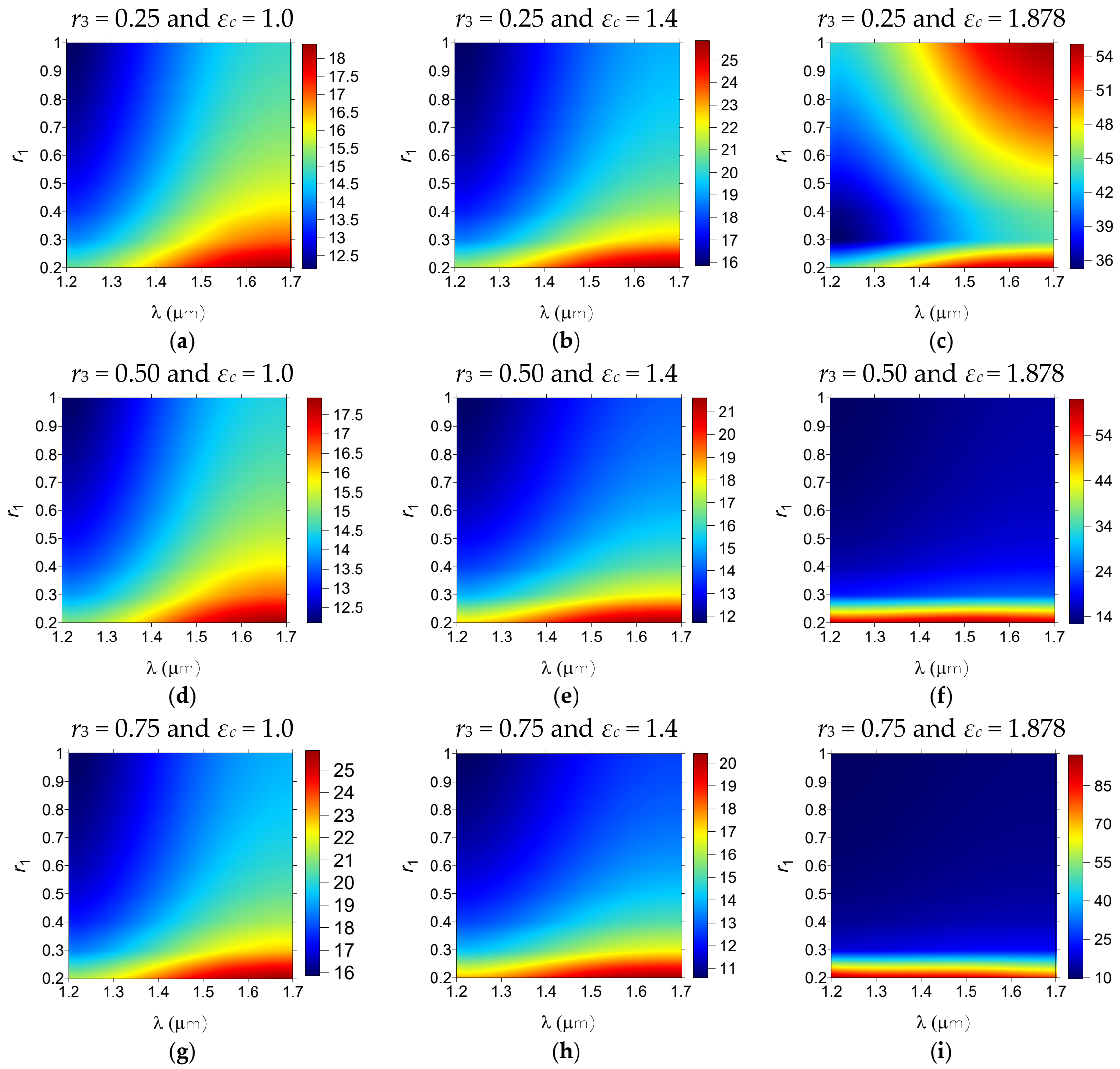

Figure 8. L in fix-asymmetric $AuAgSiO_2$ HIH-WG, fixed d = 30 nm. The waveguide parameters are (**a**) r_3 = 0.25 and ε_c = 1.0; (**b**) r_3 = 0.25 and ε_c = 1.4; (**c**) r_3 = 0.25 and ε_c = 1.878; (**d**) r_3 = 0.50 and ε_c = 1.0; (**e**) r_3 = 0.50 and ε_c = 1.4; (**f**) r_3 = 0.50 and ε_c = 1.878; (**g**) r_3 = 0.75 and ε_c = 1.0; (**h**) r_3 = 0.75 and ε_c = 1.4; (**i**) r_3 = 0.75 and ε_c = 1.878.

4. Conclusions

This work introduces a new class of planar fully asymmetric HIH waveguides for engineered light propagation in integrated photonic systems. Driven by rapid progress in nanometric thin-film fabrication, hyperbolic metamaterials (HMMs) have become powerful platforms for extreme dispersion engineering and subwavelength control of light. Within this context and based on an effective medium theory (EMT) description of multilayer optical media, we extend the notion of asymmetry beyond structural imbalance in the cladding to include the intrinsic field asymmetry of dielectric slab waveguides, establishing full asymmetry as a unified design principle.

Our results demonstrate that this generalized asymmetry provides a highly effective route to tailor and significantly enhance propagation performance. Fully asymmetric

HIH waveguides exhibit strongly tunable modal behavior, enabling propagation lengths approaching 400 µm across the C-band of optical telecommunications in optimized configurations. This level of performance highlights the potential of asymmetric metamaterial engineering as a robust strategy for overcoming traditional trade-offs between confinement and loss.

Overall, in the analyzed waveguides, we can observe long propagation distances even in configurations different from the MIM waveguide. Traditional MIM waveguides suffer from energy dissipation, and the propagation relies on Surface Plasmon Polaritons (SPPs) bound to metallic boundaries, where continuous field penetration into the metal causes Joule heating and ohmic losses, and their operating frequency is highly related to the plasmon resonances of the metals used in their composition, on the other hand [8–10].

The proposed asymmetric metamaterial claddings can be built using hybrid low-loss systems, considering material combinations including polymers with charge concentrations to shape the propagating mode size and confine the light, reducing losses. This structural optimization extends propagation lengths by orders of magnitude [8].

Integrated optics usually faces a trade-off between mode size, mode shape, and propagation loss. Asymmetric metamaterial claddings break this constraint through engineered anisotropy. This artificial anisotropy reduces the evanescent skin depth, forcing the fields to decay almost instantly at the core-cladding boundary. As a result, the optical mode remains within a subwavelength core even when its core dimensions are a fraction of the operating wavelength, achieving the ultra-compact footprint of MDM guides without the loss penalty [8,10].

Metamaterial waveguides can exhibit the same propagation properties over a large interval of frequencies (broadband operation) and can overcome MDM waveguides' limitations imposed by the narrow plasma frequency window of native metals. This may cause strong dispersion, localized resonance peaks, and a restricted operational bandwidth. The presence of metamaterial claddings overcomes this because their optical response is governed by subwavelength geometric patterning rather than rigid atomic resonances. This results in waveguides with a highly uniform, flat spectral response that spans all the optical communications Windows covering the O-E-C-L-U bands.

Metamaterial waveguides also open the possibility of obtaining dynamic tunability. Once fabricated, the dielectric properties of native metals in MIM setups are completely fixed. Metamaterial configurations, however, can integrate stimuli-responsive materials such as graphene monolayers, phase-change materials, or liquid crystals into their subwavelength gaps. Applying an external bias voltage alters the carrier density of these embedded layers, dynamically reconfiguring the tensor properties of the asymmetric cladding. This grants real-time control over the waveguide's effective refractive index, group velocity, losses, and polarization states on a single chip [18,21,27]. In addition, the metamaterial-cladded waveguides can support both TE and TM Modes simultaneously.

The most critical advantage of a metamaterial-cladded waveguide over MIM architectures is polarization versatility. In subwavelength MIM channels, the parallel metallic boundaries force the electric fields parallel to the plates to vanish. Consequently, MDM waveguides block Transverse Electric (TE) waves and only guide Transverse Magnetic (TM) plasmonic modes. Metamaterial claddings do not act as infinite electron pools, meaning they do not short out transverse electric fields. allowing the waveguide to support both TE and TM modes concurrently, allowing applications for on-chip polarization division multiplexing and complex polarization routing [21].

Finally, the introduction of asymmetry results in an additional degree of freedom to design and tailor the propagation properties of the metamaterial waveguides, adjusting the mode size and mode shape.

Author Contributions: Conceptualization, V.F.R.E. and Z.L.; Methodology, J.C.d.S., V.F.R.E., and Z.L.; Numerical Data Analysis, J.C.d.S.; Writing—original draft preparation, J.C.d.S. and V.F.R.E.; Writing—review and editing, J.C.d.S. and V.F.R.E. Investigation and Validation, J.C.d.S. and V.F.R.E.; Preparation, creation and/or presentation of the published work, specifically visualization/data presentation, J.C.d.S. and V.F.R.E.; Conducting a research and investigation process, specifically performing the experiments, or data/evidence collection, J.C.d.S.; Acquisition of the financial support for the project leading to this publication, V.F.R.E.; Oversight and leadership responsibility for the research activity planning and execution, including mentorship external to the core team, V.F.R.E. and Z.L. All authors have read and agreed to the published version of the manuscript.

Funding: This research was supported by National Council for Scientific and Technological Development (CNPQ) Processes [303795/2022-0 and 407612/2025-4], Coordination for the Improvement of Higher Education Personnel (CAPES), Bahia State Research Support Foundation (FAPESB) Process [PIE0003/2022], and Federal University of Bahia (UFBA).

Institutional Review Board Statement: Not applicable.

Informed Consent Statement: Not applicable.

Data Availability Statement: The original contributions presented in this study are included in the article. Further inquiries can be directed to the corresponding author.

Conflicts of Interest: The authors declare no conflicts of interest.

References

1. Marcuse, D. *Theory of Dielectric Optical Waveguides*; Academic Press: New York, NY, USA, 1974.
2. Okamoto, K. *Fundamentals of Optical Waveguides*; Academic Press: New York, NY, USA, 2000.
3. Maier, S.A. *Plasmonics: Fundamentals and Applications*; Springer: Berlin, Germany, 2007.
4. Bozhevolnyi, S.I. *Plasmonic Nanoguides and Circuits*; Pan Stanford Publishing: Singapore, 2008.
5. Krasavin, A.V.; Zayats, A.V. Silicon-based plasmonic waveguides. *Opt. Express* **2010**, *18*, 11791–11799. [CrossRef] [PubMed]
6. Guo, Z.; Song, J.; Jiang, H.; Chen, H. Miniaturized Backward Coupler Realized by the Circuit-Based Planar Hyperbolic Waveguide. *Adv. Photon. Res.* **2021**, *2*, 2100035. [CrossRef]
7. Guo, Z.; Long, Y.; Jiang, H.; Ren, J.; Chen, H. Anomalous unidirectional excitation of high-k hyperbolic modes using all-electric metasources. *Adv. Photon.* **2021**, *3*, 036001. [CrossRef]
8. Ishii, S.; Shalaginov, M.Y.; Babicheva, V.E.; Boltasseva, A.; Kildishev, A.V. Plasmonic waveguides cladded by hyperbolic metamaterials. *Opt. Lett.* **2014**, *39*, 4663–4666. [CrossRef] [PubMed]
9. Babicheva, V.E.; Shalaginov, M.Y.; Ishii, S.; Boltasseva, A.; Kildishev, A.V. Finite-width plasmonic waveguides with hyperbolic multilayer cladding. *Opt. Express* **2015**, *23*, 9681–9689. [CrossRef] [PubMed]
10. Babicheva, V.E.; Shalaginov, M.Y.; Ishii, S.; Boltasseva, A.; Kildishev, A.V. Long-range plasmonic waveguides with hyperbolic cladding. *Opt. Express* **2015**, *23*, 31109–31119. [CrossRef] [PubMed]
11. Babicheva, V.E. Long-range propagation of plasmons and phonon polaritons in hyperbolic-metamaterial waveguides. *J. Opt.* **2017**, *19*, 124013. [CrossRef]
12. He, Y.; He, S.; Gao, J.; Yang, X. Nanoscale metamaterial optical waveguides with ultrahigh refractive indices. *J. Opt. Soc. Am. B* **2012**, *29*, 2559–2566. [CrossRef]
13. Liang, S.; Jiang, C.; Yang, Z.; Li, D.; Zhang, W.; Mei, T.; Zhang, D. Plasmonic slow light waveguide with hyperbolic metamaterials claddings. *J. Opt.* **2018**, *20*, 065001. [CrossRef]
14. Gric, T. Surface-plasmon-polaritons at the interface of nanostructured metamaterials. *Prog. Electromagn. Res. M* **2016**, *46*, 165–172. [CrossRef]
15. Shaidiuk, V.; Menabde, S.; Park, N. Effect of structural asymmetry on three-layer plasmonic waveguide properties. *J. Opt. Soc. Am. B* **2016**, *33*, 963. [CrossRef]
16. Zhang, X.; Ren, X. Asymmetric hybrid plasmonic waveguides with cm-scale propagation length under subwavelength confinement for photonics. *Nanoscale Res. Lett.* **2014**, *9*, 599. [CrossRef]
17. Babicheva, V.E.; Shalaginov, M.Y.; Ishii, S.; Boltasseva, A.; Kildishev, A.V. Towards CMOS-compatible nanophotonics: Ultra-compact modulators using alternative plasmonic materials. *Opt. Express* **2015**, *23*, 31109–31119. [CrossRef] [PubMed]
18. Zhu, B.; Ren, G.; Zheng, S.; Lin, Z.; Jian, S. Nanoscale dielectric–graphene–dielectric tunable infrared waveguide with ultrahigh refractive indices. *Opt. Express* **2013**, *21*, 17089–17090. [CrossRef] [PubMed]
19. Tong, X.C. *Advanced Materials for Integrated Optical Waveguides*; Springer International Publishing: Cham, Switzerland, 2014.

20. Malureanu, R.; Lavrinenko, A. Ultra-thin films for plasmonics: A technology overview. *Nanomater. Rev.* **2015**, *4*, 259–275. [CrossRef]
21. Xu, H.; Dai, D.; Shi, Y. Anisotropic metamaterial-assisted all-silicon polarizer with415-nm bandwidth. *Photonics Res.* **2019**, *7*, 1432–1439. [CrossRef]
22. Teng, D.; Tian, Y.; Hu, X.; Guan, Z.; Gao, W.; Li, P.; Fang, H.; Yan, J.; Wang, Z.; Wang, K. Sodium-based cylindrical plasmonic waveguides in the near-infrared. *Nanomaterials* **2022**, *12*, 1950. [CrossRef] [PubMed]
23. Jafari, M.R.; Ghanaati, M.; Asadi, A. The characteristics of nickel-based elliptical cylinder plasmonic nano-waveguides in the near-infrared wavelength. *J. Interfaces Thin Film. Low Dimens. Syst.* **2024**, *8*, 803–810.
24. Tian, Y.; Zhang, R.; Teng, D. Cylindrical composite hybrid plasmonic waveguides with ultra-strong field confinements: A FEM study. *Plasmonics* **2025**, *20*, 595–604. [CrossRef]
25. Jafari, M.R.; Asadi, A.; Shahmansouri, M. Ultra-deep subwavelength confinement palladium-based elliptical cylinder plasmonic waveguide in the near-infrared range. *Plasmonics* **2023**, *18*, 1037–1045. [CrossRef]
26. Asadi, A. Design of multilayer graphene metamaterials plasmonic waveguides with ultra-low-loss mid-infrared. *Optik* **2025**, *327*, 172327. [CrossRef]
27. Asadi, A.; Jafari, M.R.; Shahmansouri, M. Simulation optimized design of graphene-based hybrid plasmonic waveguide. *Indian J. Phys.* **2023**, *97*, 2515. [CrossRef]
28. Ferrari, L.; Wu, C.; Lepage, D.; Zhang, X.; Liu, Z. Hyperbolic metamaterials and their applications. *Prog. Quantum Electron.* **2015**, *40*, 1–40. [CrossRef]
29. Shekhar, P.; Atkinson, J.; Jacob, Z. Hyperbolic metamaterials: Fundamentals and applications. *Nano Converg.* **2014**, *1*, 14. [CrossRef] [PubMed]
30. Choy, T.C. *Effective Medium Theory*; Oxford University Press: Oxford, UK, 2016.
31. Rodriguez-Esquerre, V.F.; da Silva, J.C.; Liu, Z. Propagation properties of metallic dielectric cladded waveguides. In Proceedings of the SPIE 9918, Metamaterials, Metadevices, and Metasystems, San Diego, CA, USA, 28 August–1 September 2016; p. 99181Z. [CrossRef]
32. da Silva, J.C.; de Figueiredo, D.A.; Rodriguez-Esquerre, V.F. Guided modes analysis in metamaterial bounded optical waveguides. In Proceedings of the SPIE 10343, Metamaterials, Metadevices, and Metasystems, San Diego, CA, USA, 6–10 August 2017; p. 103432R. [CrossRef]
33. Silva, J.C.; Rodriguez-Esquerre, V.F. Metamaterial waveguides as integrated optics sensor. *Optik* **2020**, *212*, 164756. [CrossRef]
34. Johnson, P.B.; Christy, R.W. Optical constants of the noble metals. *Phys. Rev. B* **1972**, *6*, 4370. [CrossRef]
35. Palik, E.D. *Handbook of Optical Constants of Solids, Part II*; Academic Press: New York, NY, USA, 1985.
36. Ni, X.; Liu, Z.; Kildishev, A.V. PhotonicsDB: Optical Constants. Available online: https://nanohub.org/resources/PhotonicsDB (accessed on 1 December 2025).
37. Dodge, M.J. Refractive properties of magnesium fluoride. *Appl. Opt.* **1984**, *23*, 1980–1985. [CrossRef] [PubMed]
38. Suwa, T.; Tomita, S.; Hosoito, N.; Yanagi, H. Magnetic properties of Fibonacci-modulated Fe–Au multilayer metamaterials. *Materials* **2017**, *10*, 1209. [CrossRef] [PubMed]